Kinetics of phase separation in ternary mixtures

Kumela Tafa, Sanjay Puri, and Deepak Kumar
School of Physical Sciences, Jawaharlal Nehru University, New Delhi 110067, India
(Received 5 July 2001; revised manuscript received 17 August 2001; published 30 October 2001)

We present detailed results from Monte Carlo simulations of the kinetics of phase separation in ternary mixtures. We focus on the case of *ABV* mixtures (where *V* denotes a vacancy) and investigate segregation kinetics resulting from *V*-mediated dynamics. We provide heuristic arguments for the existence of different morphologies in various parameter regimes. Furthermore, we present comprehensive numerical results for various characteristic features of the domain growth process, e.g., real-space correlation functions, domain-size distribution functions, and growth laws.

DOI: 10.1103/PhysRevE.64.056139 PACS number(s): 64.60.−i

I. INTRODUCTION

Much recent interest has focused on the kinetics of phase separation of homogeneous multicomponent mixtures, which have been rendered thermodynamically unstable by a rapid change of parameters, e.g., temperature [1–3]. Studies in this area have primarily focused on two-component or binary (AB) mixtures. In that case, the evolving system segregates into *A*- and *B*-rich domains with a characteristic length scale $L(t)$, where t is the time after the quench. These domains coarsen with time because it is energetically favorable to eliminate domain boundaries. The coarsening mechanisms can be either diffusive (e.g., binary alloys) or hydrodynamic (e.g., binary fluids), and the domain growth law depends on the relevant coarsening mechanism [3]. If growth is driven by diffusion, we have $L(t)\sim t^{1/3}$ for dimensionality $d\geqslant 2$, which is referred to as the Lifshitz-Slyozov (LS) growth law [4]. If the primary growth mechanism is hydrodynamic, we have $L(t)\sim t^{x}$, where x takes a range of different values—depending on the time regime and the dimensionality [5,3].

There have been many experiments and numerical simulations of phase separation in binary mixtures, and these have greatly enhanced our understanding of this problem. At the analytical level, we have a good understanding of various mechanisms for domain growth and the resultant growth laws [3]. However, more quantitative attempts to characterize the morphology using the real-space correlation function (or its Fourier transform, the momentum-space structure factor) have met with limited analytical success–except in the limit where one of the components is present in a vanishingly small fraction [4].

Apart from domain growth laws and morphology, it is also relevant to examine the autocorrelation function in the far-from-equilibrium evolution of the phase-separating system. There are very few studies of this experimentally relevant quantity [6,7]. Marko and Barkema (MB) [6] have presented numerical results for the autocorrelation function $\Phi(t_0,t)$ in the phase separation of binary mixtures, with t_0 being an initial reference time. MB argue that their numerical data is consistent with a power-law decay $\Phi(t_0,t)\sim(t_0/t)^{\theta}$, where the value of θ depends on whether or not t_0 is in the scaling regime. For t_0 in the scaling regime, MB report that $\theta\simeq 1.0$ for $d=2$ and $\theta\simeq 0.5$ for $d=3$.

In this paper, we undertake a comprehensive Monte Carlo (MC) study of phase-separation kinetics in three-component or ternary (ABC) mixtures. To date, there has been only limited investigation of these systems, which are of great experimental significance. In particular, we will focus on the range of possible morphologies of the segregating mixture, and the corresponding dynamical behaviors, as characterized by various standard tools.

In a more general context, our study is relevant for systems with two coupled order parameters, e.g., ^{3}He-^{4}He mixtures, binary alloys with one ferromagnetic component, etc. Clearly, the underlying phase diagrams and domain morphologies in these systems are considerably more complex than for systems with a single-order parameter. It is of obvious interest to study domain coarsening in different regimes of the phase diagram. An interesting feature is the existence of two types of domain morphologies in the regime of three-phase coexistence. We show that the existence of these morphologies can be understood using simple energetic arguments.

This paper is organized as follows. In Sec. II, we provide an overview of earlier studies of phase separation in ternary mixtures. This overview will provide the context for our present study. In Sec. III, we provide a brief discussion of the phase diagrams and domain morphologies that are relevant for our dynamical studies. In Sec. IV, we present detailed results for characteristic properties of phase-separating ternary mixtures. Finally, Sec. V concludes this paper with a summary and discussion of our results.

II. OVERVIEW OF EARLIER STUDIES

As a prelude to our discussion of earlier studies, it is convenient to introduce the model Hamiltonian for a ternary mixture. We consider a ternary (ABC) mixture on a discrete lattice (having cubic symmetry) with N sites, and assume that there are only nearest-neighbor interactions with strength $\epsilon_{\alpha\beta}$ between species α and β. (We take $\epsilon_{\alpha\beta}=\epsilon_{\beta\alpha}$.) The appropriate Hamiltonian is

$$H=\sum_{\alpha,\beta}\epsilon_{\alpha\beta}\sum_{\langle ij\rangle}n_i^{\alpha}n_j^{\beta}-\sum_{\alpha}\mu_{\alpha}\sum_{i}n_i^{\alpha}, \qquad (1)$$

where $n_i^{\alpha}\in\{0,1\}$ refers to the occupation number for species α at site i, the variables α and β take three values, corre-

sponding to elemental species A, B, C, and $\Sigma_{\langle ij\rangle}$ refers to a sum over nearest-neighbor pairs. We also include chemical potential terms, with μ_α denoting the chemical potential of species α, as this gives us the flexibility to choose the best ensemble to obtain relevant phase diagrams. As usual, we have the constraint $n_i^A+n_i^B+n_i^C=1$.

It is convenient to map this Hamiltonian into that for a spin-1 model [8–10]. We introduce the spin variable $s_i \in\{-1,0,1\}$, and define

$$n_i^A=\frac{s_i^2+s_i}{2},$$

$$n_i^B=\frac{s_i^2-s_i}{2},$$

$$n_i^C=1-s_i^2. \tag{2}$$

In terms of the spin variables, the Hamiltonian assumes the form

$$H=-J\sum_{\langle ij\rangle} s_i s_j-K\sum_{\langle ij\rangle} s_i^2 s_j^2-\frac{M}{2}\sum_{\langle ij\rangle}(s_i^2 s_j+s_i s_j^2)$$

$$-\sum_i (hs_i+\Delta s_i^2). \tag{3}$$

The interaction parameters in Eq. (3) are identified as [10]

$$J=\frac{2\epsilon_{AB}-\epsilon_{AA}-\epsilon_{BB}}{4},$$

$$K=\frac{4(\epsilon_{AC}+\epsilon_{BC}-\epsilon_{CC})-2\epsilon_{AB}-\epsilon_{AA}-\epsilon_{BB}}{4},$$

$$M=\frac{2(\epsilon_{AC}-\epsilon_{BC})-\epsilon_{AA}+\epsilon_{BB}}{2},$$

$$h=\frac{q(\epsilon_{BC}-\epsilon_{AC})+\mu_A-\mu_B}{2},$$

$$\Delta=\frac{2q(\epsilon_{CC}-\epsilon_{AC}-\epsilon_{BC})+\mu_A+\mu_B-2\mu_C}{2}, \tag{4}$$

where q is the number of nearest neighbors (coordination number) of a lattice site. Equation (3) is the most general form of the Blume-Emery-Griffiths Hamiltonian [8], first proposed to study phase separation and superfluid ordering in ^{3}He-^{4}He mixtures. There have been many subsequent studies of the phase diagram of this Hamiltonian [10–13].

We are interested in the dynamical properties of this Hamiltonian in conjunction with an appropriate microscopic conserved kinetics. There have already been a few numerical studies of phase-separation kinetics for this Hamiltonian with fixed numbers of each species, and we would like to briefly summarize representative results here. In the context of fixed composition, the terms involving $\Sigma_i s_i$ and $\Sigma_i s_i^2$ in the Hamiltonian of Eq. (3) are constant and need not be considered.

Most earlier dynamical studies of this Hamiltonian have been in the context of the ABV model, where $C\equiv V$ (or vacancy) and there are no pairwise interaction terms involving vacancies. Our present study also falls into this category. This model is of great relevance in the context of vacancy-mediated phase separation in alloys, where it is known that the relevant physical processes that enables segregation are $A\leftrightarrow V$ and $B\leftrightarrow V$ interchanges rather than $A\leftrightarrow B$ interchanges [14,15]. We should stress that, in the context of the equilibrium phase diagram, the ABV model already gives rise to the most general spin-1 Hamiltonian in Eq. (3).

Some early MC studies of the $d=2$ ABV model are due to Yaldram and Binder (YB) [16], who investigated the evolution morphologies arising for three sets of parameter values. In each case, there was segregation in A- and B-rich domains. The different morphologies are characterized by the distribution of V's as follows:

(i) $J=\epsilon/2$, $K=-\epsilon/2$, $M=0$ where ϵ is an energy scale. In this case, the vacancies were uniformly and randomly distributed throughout the system.

(ii) $J=\epsilon/2$, $K=\epsilon/2$, $M=0$. In this case, the vacancies were expelled from bulk A- and B-domains and tended to aggregate in AB interfacial regions. However, all possible interfaces (AV, BV, and AB) were present in the evolution morphology.

(iii) $J=\epsilon/2$, $K=\epsilon/2$, $M=\epsilon$. In this case, the vacancies were completely expelled from A-rich regions and macroscopic V-rich domains were observed.

YB also made some preliminary studies of the quantitative features of domain morphologies, but these did not probe the intermediate or late-stage behavior. Subsequently, we will present heuristic arguments to systematize the YB observation of different morphologies.

Another important MC study of this problem is due to Fratzl and Penrose (FP) [17], who considered segregation in an AB mixture mediated by a single vacancy. FP found that domain growth mediated by a single vacancy is more rapid than domain growth via the usual Kawasaki exchange mechanism ($A\leftrightarrow B$). Furthermore, the asymptotic domain growth law in their study is consistent with the LS growth law, $L(t)\sim t^{1/3}$. However, we should stress that the FP study differs from the YB study (and also our present study) in that a single vacancy is irrelevant in the thermodynamic limit. Thus, the appropriate equilibrium phase diagram for the FP study is the usual one for a binary mixture.

In more recent work, Puri and Sharma (PS) [18,19] have formulated mean-field (MF) dynamical models for vacancy-mediated phase separation. These models consider the coupled dynamics of two conserved order parameters (viz., $\langle s_i\rangle$ and $\langle s_i^2\rangle$), and classify as ''Model D'' in critical-dynamics terminology [20–22]. PS studied these models both numerically and analytically, and reported comprehensive numerical results for the case $K=M=0$—corresponding to the case of a spin-1 Ising model. They found that the vacancies aggregated at the AB interfaces, thereby reducing the surface tension. However, domain growth is still consistent with the LS law, and the vacancy layer at the interfaces does not impede phase separation. Plapp and Gouyet [23,13] have also formulated simi-

lar MF dynamical models for the ABV model, and have used them to investigate surface instabilities for droplets of the unstable mixture immersed in a stable vapor of the mixture.

In the above works, the V concentration is usually small as this is appropriate in the physical context of vacancy-mediated phase separation in binary alloys. A complementary set of works has focused on segregation dynamics in n-state Potts models, where the different components of the mixture are treated on equal footing. The three-state Potts model can be formulated as the spin-1 Hamiltonian in Eq. (3) with parameters $J=\epsilon/2$, $K=3\epsilon/2$, $M=0$. Jeppesen and Mouritsen (JM) [24] performed a MC study of the three-state Potts model with Kawasaki spin-exchange (conserved) kinetics. These authors considered ''critical quench'' conditions with all components being present in equal proportions. In the JM study, the evolving morphology is characterized by distinct domains rich in either of the components with all types of interfaces present. We will later refer to this as the ''blob'' morphology. JM find that the asymptotic domain growth law is the LS law, correcting an earlier result of Grest and Sahni [25], who found effectively lower growth exponents due to transient effects. The numerical results of JM have been confirmed in a recent exchange MC study by Okabe [26].

Finally, we would like to briefly discuss an important set of studies examining the effect of surfactants (S) on segregation dynamics of binary mixtures (AB). This system also constitutes a ternary mixture (ABS) with the third component (i.e., surfactant) being present in a small fraction—as in the case of vacancies in the ABV model. Typically, the component S aggregates at AB interfaces and lowers the AB surface tension, so that the evolving system freezes into a microstructure. A number of reviews and studies [27–29] have discussed the kinetics of phase separation in ABS mixtures and we refer the interested reader to these.

III. MEAN-FIELD PHASE DIAGRAMS

In this section, we briefly review the thermodynamics of the system and present MF phase diagrams in the parameter ranges relevant to our dynamical studies. We will consider temperature quenches that are far from phase boundaries–hence, MF phase diagrams suffice to describe the different phases observed. All results reported in this paper are for the Hamiltonian in Eq. (3) with $M=0$. We fix the number of species A and B to be equal, i.e., $N_A=N_B$. Under these conditions, symmetry requires that all phase transitions occur at $h=0$. Physically, the interaction J drives phase separation between A and B, while the interaction K (if positive) drives phase separation between V and A, B. To understand the above situation, it is useful to invoke the magnetic alloy analogy, where the A and B species are interpreted as ''up'' and ''down'' spins of a ferromagnetic element; and V is a nonmagnetic component. Then, J drives the paramagnetic to ferromagnetic transition, while K (if positive) drives phase separation between the magnetic and nonmagnetic components.

Since we are using conserved kinetics, the appropriate ensemble for studying the phase diagram is the fixed-(T,m,ρ) ensemble, where T is the temperature; and the order parameters are $m=\langle s_i\rangle$ and $\rho=\langle s_i^2\rangle$. The corresponding free energy in the MF approximation is

$$\frac{F(T,m,\rho)}{N}=-\frac{qJ}{2}m^2-\frac{qK}{2}\rho^2+T\left[\frac{\rho+m}{2}\ln\left(\frac{\rho+m}{2}\right)+\frac{\rho-m}{2}\ln\left(\frac{\rho-m}{2}\right)+(1-\rho)\ln(1-\rho)\right], \quad (5)$$

where the third term on the right-hand side is the entropy per spin ($k_B=1$). The free energy in Eq. (5) can be used to obtain qualitative features of the phase diagram and has been extensively investigated [8,10–13].

A simple method of obtaining the MF phase diagram proceeds by first considering the relevant phase diagram in the fixed-$(T,h=0,\mathbf{\Delta})$ ensemble. This is obtained by solving the following coupled transcendental equations for m and ρ [8],

$$m=\frac{2\sinh(q\beta Jm)}{\exp[-\beta(qK\rho+\mathbf{\Delta})]+2\cosh(q\beta Jm)},$$

$$\rho=\frac{2\cosh(q\beta Jm)}{\exp[-\beta(qK\rho+\mathbf{\Delta})]+2\cosh(q\beta Jm)}. \quad (6)$$

An obvious root of Eq. (6) is $(m_0=0,\rho_0)$, where ρ_0 solves the transcendental equation

$$\rho_0=\frac{2}{\exp[-\beta(qK\rho_0+\mathbf{\Delta})]+2}. \quad (7)$$

In general, Eq. (6) is solved numerically to obtain the following features: (a) A line of second-order transitions, which is characterized by the emergence of three roots $(0,\rho_0)$, $(\pm m_s,\rho_s)$ continuously from the single root $(0,\rho_0)$. The equation of this line in the $(T,\mathbf{\Delta})$ plane is $\mathbf{\Delta}=-T\ln[2(q\beta J-1)]-TK/J$ [8]. (b) A line of first-order transitions, which is characterized by the emergence of five roots $(0,\rho_0)$, $(\pm m_1,\rho_1)$, $(\pm m_2,\rho_2)$ with the free energy associated with $(\pm m_2,\rho_2)$ $(m_2>m_1)$ becoming lower than that associated with $(0,\rho_0)$. The relevant free energy is the Legendre transform of $F(T,m,\rho)$ in Eq. (5), i.e., $G(T,h,\mathbf{\Delta})=F(T,m,\rho)-hm-\mathbf{\Delta}\rho$. The line of first-order transitions starts from $[T=0,\ \mathbf{\Delta}=-q(J+K)/2]$ and meets the second-order line in the tricritical point $(T_t,\mathbf{\Delta}_t)$. An approximate equation for this first-order line can be obtained in the framework of Landau theory.

It is straightforward to map the phase diagram in the $(T,h=0,\mathbf{\Delta})$-plane into phase diagrams with fixed composition by computing the values of composition variables either side of the first-order transition line. The appropriate phase diagrams in the $(T,h=0,\rho)$ plane are shown in Figs. 1(a)–1(c) for $d=2$ $(q=4)$ and $K=1.5,0.5,-0.5$. (All energy scales are subsequently measured in units of J, i.e., $J=1$.) These phase diagrams are appropriate in the context of a binary alloy where one of the components is ferromagnetic [8]. They will also serve as a useful reference point for the dynamical simulations described subsequently.

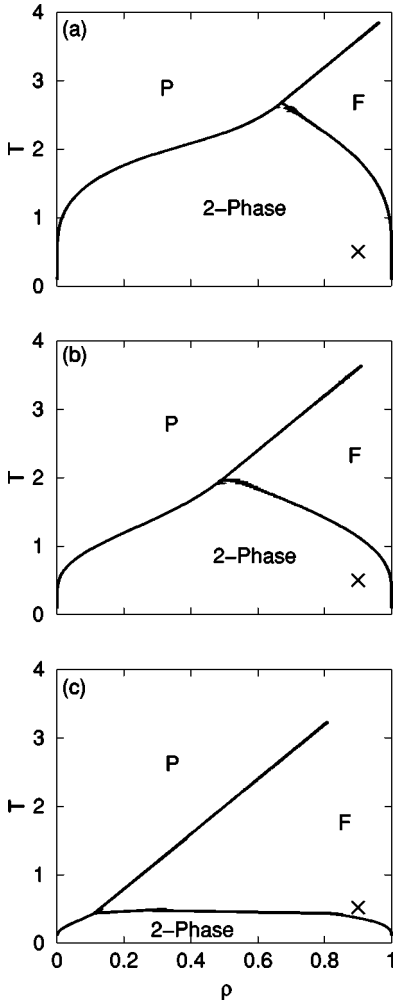

FIG. 1. Mean-field (MF) phase diagrams in the $(T,h=0,\rho)$ plane for the Hamiltonian in Eq. (3) with $M=0$. The labels P and F refer to the paramagnetic and ferromagnetic phases, respectively. All parameters are measured in units of J, i.e., $J=1$. We show phase diagrams for (a) $K=1.5$, (b) $K=0.5$, and (c) $K=-0.5$. The parameter values for our dynamical simulations are marked as X's in (a)–(c).

In Fig. 1, for $\rho=1$, there is a second-order transition from the paramagnetic to ferromagnetic phase at the temperature $T_c(1)=q$. To begin with, as ρ is decreased the transition temperature $T_c(\rho)$ also decreases, i.e, $T_c(\rho)=q\rho$. In the ferromagnetic phase that results, we have a two-phase region with up (A-rich) and down (B-rich) domains with V atoms distributed uniformly. This continues with decreasing ρ, till one reaches the tricritical point (T_t,ρ_t), where the second-order transition becomes first-order transition, as there is a phase separation between ferromagnetic (AB-rich) and nonmagnetic (V-rich) components. The ferromagnetic component retains the magnetic order, thus here we have a three-phase coexistence. As seen in Fig. 1, larger values of K raise the tricritical point as phase separation is favored, while lower values of K have the reverse effect.

We study the dynamics of the ABV system using Kawasaki spin-exchange kinetics (with Metropolis acceptance rates), which individually conserves numbers of A $(s_i=1)$, B $(s_i=-1)$, and V $(s_i=0)$. We further put a constraint on the kinetics that permits only V-mediated dynamics, i.e., $A\leftrightarrow V$ and $B\leftrightarrow V$ interchanges are permitted but not $A\leftrightarrow B$ interchanges. However, in contrast to most earlier works, we have studied physical situations with appreciable V concentrations so as to investigate domain coarsening in both regions of the phase diagram, namely regions with two-phase and three-phase coexistence. The quenches we consider in our simulations are marked as X's in the phase diagrams of Fig. 1—we always consider the symmetric case with $N_A=N_B$ or $m=0$.

IV. NUMERICAL RESULTS

Our MC simulations were performed on N^2 lattices (i.e., dimensionality $d=2$) with periodic boundary conditions in both directions. The results presented here use a sequential updating procedure but similar results are obtained with random updates. The initial condition for each run consisted of a randomly distributed mixture of 0's, ± 1's, mimicking the homogeneous initial state at high temperatures. The system is then evolved at a quenched temperature in the multiphase region, so that it is in a far-from-equilibrium state. For the results presented in this paper, the concentrations of A, B, and V were $c_A=c_B=0.45$, $c_V=0.1$. As mentioned earlier, all energy scales are measured in units of J. We fix the temperature $T=0.5$, and vary the parameter K. We stress that the results presented here are generic (up to prefactors and time scales) for a wide range of compositions and temperatures.

We will show numerical results for various evolution morphologies and their time-dependent properties. The statistical features we focus on are as follows: (a) correlation functions of the two order parameters, i.e., s_i and s_i^2; (b) domain-size distribution functions; and (c) characteristic domain length scales. We will provide precise definitions of these quantities subsequently. All statistical quantities are calculated as an average over ten independent runs for system sizes $N=512$.

A. Domain morphologies

Let us start by showing typical evolution morphologies from a random initial condition. Figures 2(a)–2(c) show evolution pictures for $K=1.5$, 0.5, and -0.5, respectively. Notice that Figs. 2(a) and 2(b) correspond to quenches into the three-phase region [see Figs. 1(a) and 1(b)], whereas Fig. 2(c) corresponds to a quench into the two-phase region [see Fig. 1(c)]. In Fig. 2(a), one sees a clear evolution of three kinds of domains, namely, A, B, and V rich. We term this as the ''blob'' (B) morphology. Here, all three kinds of interfaces (AV, BV, and AB) are present. The evolution in Fig. 2(b) also corresponds to the three-phase region, but the parameter values are closer to the phase boundary with the two-phase region. Here, we see that A- and B-rich domains are separated by a thin layer of V's. We term this as the ''coated'' (C) morphology. The thickness of the coating layer of V's does not grow in time. The excess V's form blobs, as we have confirmed from simulations at higher concentrations of V. The distinct feature of this regime is the absence of AB interfaces.

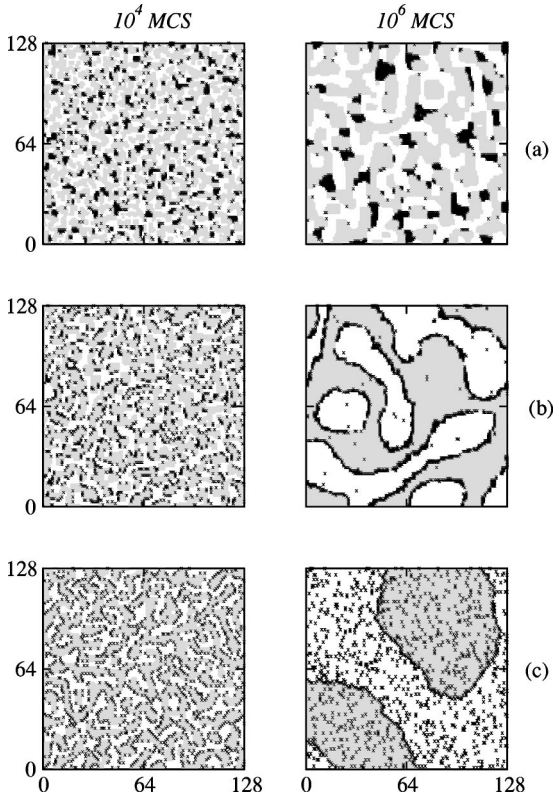

FIG. 2. Evolution pictures for the spin-1 model with vacancy-mediated spin-exchange kinetics. Our Monte Carlo (MC) simulations were performed on N^2 lattices ($N=512$) with periodic boundary conditions in both directions. The initial condition for each run consisted of a random mixture of A, B, V with $c_A=c_B=0.45$ and $c_V=0.1$. In the evolution pictures, A's are marked in gray; B's are unmarked; and V's are marked as X's. The snapshots are labeled by the appropriate evolution time subsequent to the quench in Monte Carlo steps (MCS). (For clarity, we only show a 128^2 corner of the evolving system.) The parameter values (measured in units of J) were $T=0.5$, and (a) $K=1.5$; (b) $K=0.5$; and (c) $K=-0.5$. Phase diagrams for these parameter values are shown in Fig. 1.

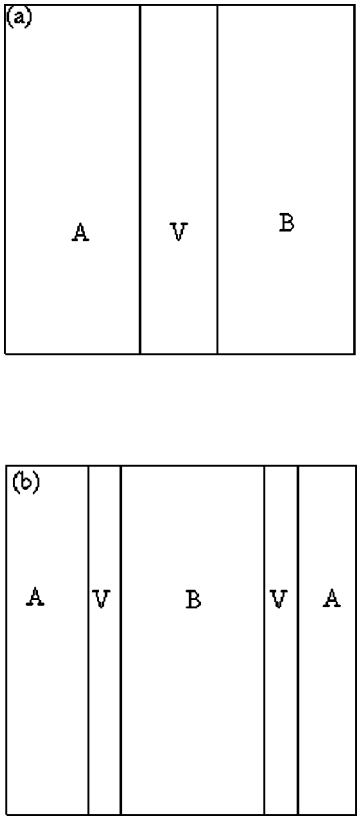

FIG. 3. Typical examples of $T=0$ morphologies for three-phase coexistence in $d=2$. (a) Blob (B), where all possible interfaces (AV, BV, and AB) are present. (b) Coated (C), where only AV and BV interfaces are present.

Finally, Fig. 2(c) shows the evolution of only two kinds of domains that are A rich and B rich with V's interspersed uniformly—as dictated by thermodynamics. This is similar to phase separation in two-component systems. This morphology will be referred to as the ''dispersed'' (D) morphology. A microscopic layer of V's does coat the AB interfaces in this regime as well. This is expected on simple energetic grounds, as shifting a vacancy from the interior of an A (or B)-rich domain to the AB interface gains an energy of 2 J. Note that this argument applies only to the two-phase regime, and V's do not form a macroscopic phase as in the C morphology. We should stress that the early-time frame in Fig. 2(c) ($t=10^4$ MCS where MCS is Monte Carlo steps) actually appears to exhibit a C-type morphology. This is because the length scales at initial times are so small that even one layer is significant. At later times, when the length scales are larger and local equilibrium is established, the phase diagram of Fig. 1 is relevant.

We next consider the reason why two distinct domain morphologies occur in the three-phase region. This can be understood from the following simple considerations at $T=0$. Consider a typical domain geometry on a square lattice of linear size L with periodic boundary conditions (Fig. 3). We focus on the case with $N_A=N_B=yL$ and $N_V=(1-2y)L$. In the ground state, we can have two possible configurations of domains as shown in Figs. 3(a) (blob) and 3(b) (coat). The configuration in Fig. 3(a) is the lowest-energy configuration of the B morphology as all possible interfaces occur only once. In the configuration of Fig. 3(b), we have distributed V's to eliminate the AB interface at the cost of forming an extra AV and BV interface. In this geometry, it is straightforward to calculate the energy of the two configurations as

$$E_B=-2Ly(J+K)+(3J+K)L,$$

$$E_C=-2Ly(J+K)+(2J+2K)L. \tag{8}$$

A comparison of the two energies shows that the B morphology is favored when $J<K$, while the C morphology is preferred when $J>K$. Though the geometrical configuration for which the above argument has been presented is rather simple, it demonstrates that an AV plus BV interface is preferred over an AB interface when $J>K$, and vice versa when $J<K$. Thus, for the same region of three-phase coexistence, different morphologies can arise depending on the ratio of the two interactions. However, we note that the coat forma-

tion of V's in excess of a couple of layers has no additional energetic advantage in the context of reducing AB surface tension. Therefore, the coat thickness is expected to saturate out to an equilibrium value, as we have confirmed numerically. Subsequent to this saturation, additional V's form blobs as this is entropically favorable. Thus, in the asymptotic time regime, there should be no difference between two-point correlation functions for B and C morphologies, as the fixed length scale of the vacancy ''wetting layer'' at AB interfaces is irrelevant compared to the divergent length scales of the A, B, and V domains. In practice, especially for small V concentrations, the crossover time to this asymptotic regime may be excessively delayed.

The above arguments, and simple extensions thereof, clarify the observation of different morphologies in earlier simulations, which were reviewed in Sec. II.

B. Correlation functions and domain-size distributions

We will now consider various statistical properties of the evolution depicted in Figs. 2(a)–2(c). We shall first present a detailed discussion for the blob morphology in Fig. 2(a). Since the discussion for other morphologies is similar, we will present briefer discussions of these, mainly highlighting differences from the blob morphology. The simplest characterization of the morphology is by two-point correlation functions and the domain-size distribution functions. Here, we have two kinds of correlation functions of spin variables. The first one is defined as follows:

$$C(r,t)=\langle s(\vec{R},t)s(\vec{R}+\vec{r},t)\rangle-\langle s(\vec{R},t)\rangle\langle s(\vec{R}+\vec{r},t)\rangle, \quad (9)$$

where $s(\vec{R},t)$ is the spin variable at a discrete site $\vec{R}$ at time t; and the angular brackets refer to an averaging over independent runs and noise realizations. This correlation function refers to the A-, B-domain morphology. The second correlation function of $s(\vec{R},t)^2$ [or $1-s(\vec{R},t)^2$] is also defined in a similar fashion as follows:

$$D(r,t)=\langle s(\vec{R},t)^2 s(\vec{R}+\vec{r},t)^2\rangle-\langle s(\vec{R},t)^2\rangle\langle s(\vec{R}+\vec{r},t)^2\rangle, \quad (10)$$

and refers to the V-domain morphology.

The domain-size distribution $P(l,t)$, where $l\in[0,\infty]$, is obtained by examining the zero crossings of order-parameter profiles along horizontal and vertical cross sections of the lattice [30]. We separately consider distributions for the A, B domains, and the V domains. The distribution $P(l,t)$ is normalized as $\int_0^\infty dl P(l,t)=1$.

Figure 2(a) suggests that the evolving morphology is self-similar in time, and we expect the correlation functions to exhibit a dynamical-scaling form $C(r,t)=g(r/L);D(r,t)=h(r/L)$, where the master functions $g(x)$ and $h(x)$ are independent of time [31]. Figure 4(a) superposes data from different times for $C(r,t)/C(0,t)$ vs r/L_C, where L_C is defined as the distance over which the correlation function decays to half its maximum value. The solid line in Fig. 4(a) refers to the scaled correlation function for the spin-1/2 Ising model with Kawasaki kinetics (also obtained numerically).

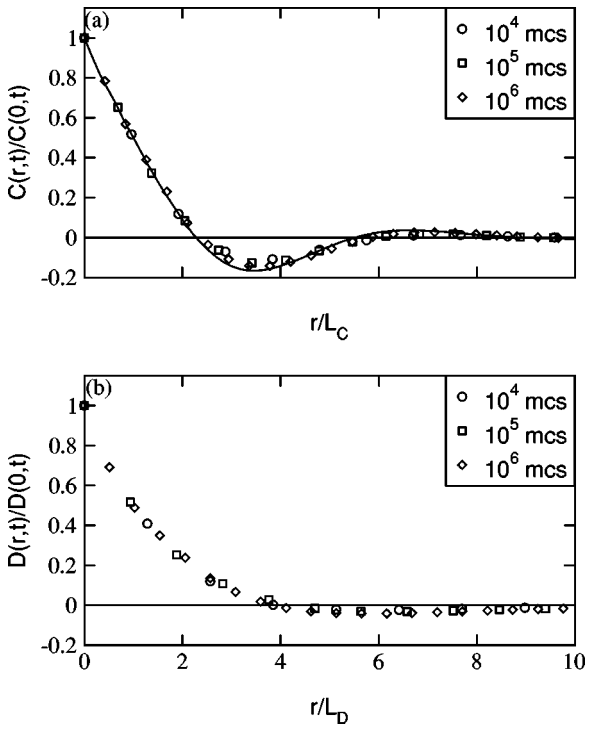

FIG. 4. Scaling plot of correlation functions for the evolution depicted in Fig. 2(a). We calculate $C(r,t)$ and $D(r,t)$ (correlation functions for the s field and s^2 field, respectively) as an average over ten independent runs on lattices of size $N=512$. (a) Plot of $C(r,t)/C(0,t)$ vs r/L_C for three different times—denoted by the symbols indicated. The length scale L_C is defined as the distance over which the correlation function decays to half its maximum value. The solid line denotes the scaled correlation function (at $t=10^6$ MCS) obtained from MC simulations of the spin-1/2 Ising model with Kawasaki spin-exchange kinetics. (b) Plot of $D(r,t)/D(0,t)$ vs r/L_D for the same times as in (a).

Because of the small V concentration ($c_V=0.1$), the correlation function for the blob morphology does not differ appreciably from that for the spin-1/2 Ising model. More substantial differences are seen when the components are present in approximately equal proportions, as in the MC simulations of the three-state Potts model by Jeppesen and Mouritsen [24]. Figure 4(b) is the corresponding scaling plot of $D(r,t)/D(0,t)$ vs r/L_D. The good data collapse in Figs. 4(a) and 4(b) confirms the dynamical scaling of the correlation functions.

The corresponding dynamical-scaling property for the domain-size distribution is $P(l,t)=L^{-1}f(l/L)$. In this paper, we focus on the distribution for A, B domains as that is physically more relevant. Figure 5 superposes data from different times for $P(l,t)L_P$ vs l/L_P, where the characteristic length scale L_P is defined from the domain distribution function as $L_P=\langle l\rangle$. (In the scaling regime, we expect L_C, L_D, and L_P to be equivalent upto prefactors.) Again, the data collapse is seen to be excellent in Fig 5(a), which is a direct plot of the data. The solid line in Fig. 5(a) is the scaled domain-size distribution for the spin-1/2 Ising model (also obtained numerically), and is in good agreement with our numerical data for the ABV model. Figure 5(b) is a linear-

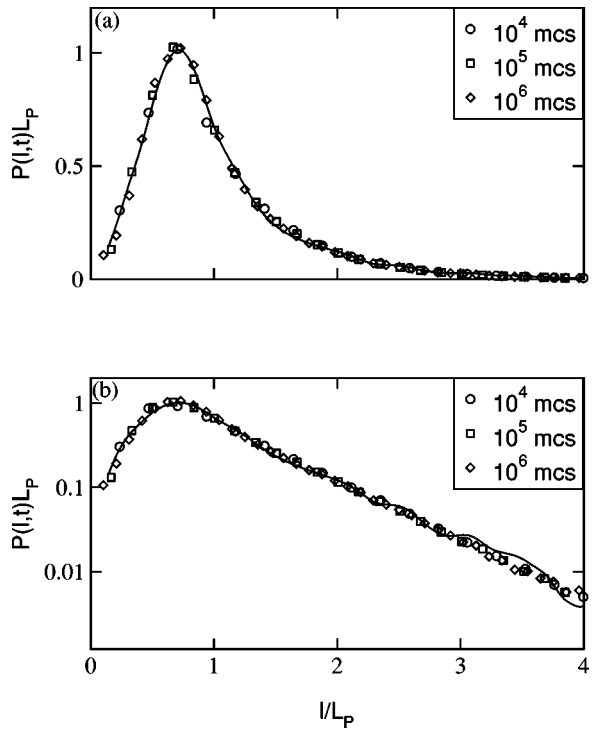

FIG. 5. Scaling plot of domain-size distributions of *A*, *B* domains for the evolution depicted in Fig. 2(a). We plot $P(l,t)L_P$ vs l/L_P for three different times—denoted by the symbols indicated. The length scale $L_P=\langle l\rangle$, i.e., the first moment of the probability distribution. The averaging statistics is the same as that for Fig. 4. The solid line denotes the scaled probability distribution for the spin-1/2 Ising model at $t=10^6$ MCS. We present the numerical data on (a) a direct plot and (b) a linear-log plot.

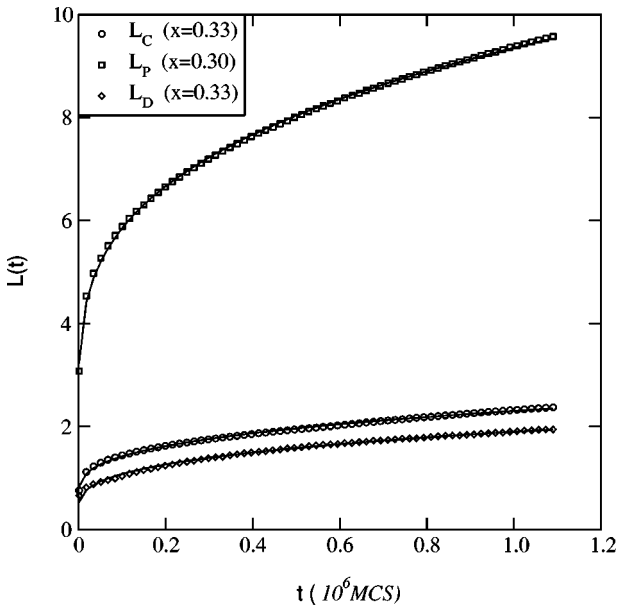

FIG. 6. Time dependence of characteristic length scales for the evolution depicted in Fig. 2(a). We plot $L(t)$ vs t for three measures of the length scale, i.e., L_C and L_P refer to the *A*-, *B*-domain scale obtained from $C(r,t)$ and $P(l,t)$, respectively; and L_D refers to the *V*-domain scale obtained from $D(r,t)$. The solid line superposed on each data set denotes the best fit to the functional form $L(t)=a+bt^x$, and the best-fit exponent x is specified on the figure. The error estimates for the exponents are ± 0.01.

log plot of the data in Fig. 5(a). The tail of the scaling function $f(y)$ exhibits a characteristic exponential decay. We have first observed this in the context of nonconserved domain growth [30] and expect it to be a universal feature of phase-ordering systems. In our earlier study of nonconserved domain growth with barriers, the exponential tail of $f(y)$ resulted in an asymptotically stretched-exponential behavior for the spin autocorrelation function [30].

Figure 6 plots $L(t)$ vs t for length scales obtained from the two correlation functions (see Fig. 4); and the domain-size distribution function (see Fig. 5). The time dependence of all the data sets is consistent with the LS growth law, $L(t)\sim t^{1/3}$.

We now turn to a quantitative discussion for the other two morphologies. Recall that Fig. 2(b) showed the evolution for parameter values $T=0.5$, $K=0.5$, which also corresponds to three-phase coexistence [see Fig. 1(b)], but with a coating morphology. The correlation functions $C(r,t)$ and $D(r,t)$ for the *C* morphology are expected to be similar to those for the *B* morphology, particularly at late times. The reason is that, as far as the two-point correlation functions are concerned, the distribution of *V*'s in both *C* and *B* morphologies becomes statistically identical in the asymptotic time regime. The finite thickness of the coating layer at *AB* interfaces is irrelevant as other length scales in the system diverge. Clearly, higher-order correlation functions are required to quantify the differences in the two-domain morphologies. In practice, especially for small *V* concentrations, the crossover time to this asymptotic regime may be excessively delayed. The final frame ($t=10^6$ *mcs*) in Fig. 2(b) shows incipient cluster formation by *V* domains. We have confirmed numerically that the onset of clustering of *V*'s is faster at higher values of the *V* concentration.

Figure 2(c) shows evolution pictures for $T=0.5$, $K=-0.5$, which corresponds to two-phase coexistence with *AV*-rich and *BV*-rich domains [see Fig. 1(c)]. There is also a microscopic layer of *V* at the *AB* interfaces, as this lowers the system energy. However, the *V*-rich layer is thermodynamically irrelevant. For these parameter values, the *V*'s play no significant role in determining the asymptotic morphology, though, of course, they do mediate the dynamics. In this regime, we expect the system evolution to be asymptotically equivalent to that for the spin-1/2 Ising model.

The correlation function data for the *C* and *D* morphologies also exhibits dynamical scaling. For brevity, we do not present this data here. Figure 7(a) superposes data for $C(r,t)/C(0,t)$ vs r/L_C from the *B*, *C*, and *D* morphologies at $t=10^6$ MCS. For reference, we also include the correlation function for the spin-1/2 Ising model–denoted as a solid line. We see that the data sets for *B* and *C* are numerically comparable; and differ from the scaled correlation function for the *D* morphology. For even larger values of c_V, the *B* and *C* morphologies should still be comparable at sufficiently late times, but would differ substantially from the D and Ising morphologies. Figure 7(b) superposes data for $D(r,t)/D(0,t)$ vs r/L_D from the *B* and *C* morphologies at

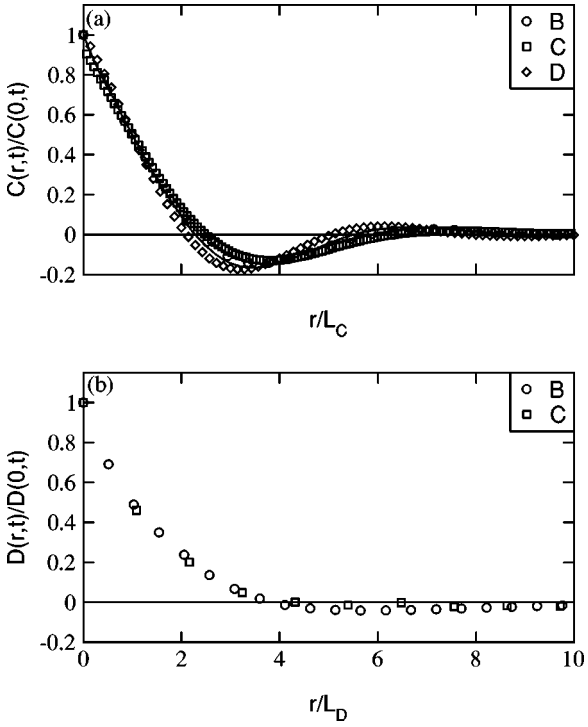

FIG. 7. (a) Superposition of numerical data for $C(r,t)/C(0,t)$ vs r/L_C for the *B*, *C*, and *D* morphologies. The solid line refers to the corresponding data for the spin-1/2 Ising model. All data sets are computed at $t=10^6$ MCS. (b) Superposition of data for $D(r,t)/D(0,t)$ vs r/L_D for the *B* and *C* morphologies. Both data sets are computed at $t=10^6$ MCS.

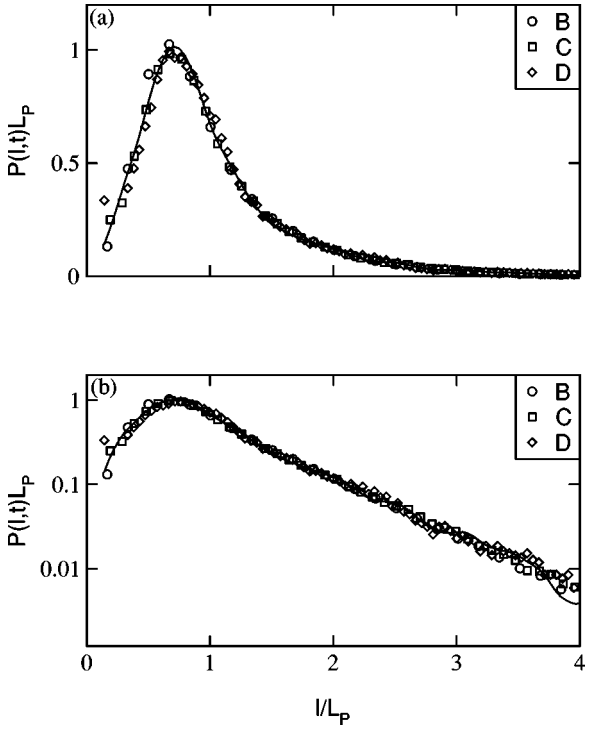

FIG. 8. (a) Superposition of data for $P(l,t)L_P$ vs r/L_P for the *B*, *C*, and *D* morphologies. The solid line refers to the corresponding data for the spin-1/2 Ising model. All data sets are computed at $t=10^6$ MCS. (b) Data from (a), replotted on a linear-log scale.

$t=10^6$ MCS (this correlation function is not meaningful in the context of the *D* morphology).

Figure 8(a) is a direct plot of data for $P(l,t)L$ vs l/L_P for the *B*, *C*, and *D* morphologies. As before, the solid line refers to the corresponding data for the spin-1/2 Ising model. For the *D* morphology, the domain-size distribution $P(l,t)$ is obtained by binarizing the evolution pictures in Fig. 2(c), i.e., a 0 is mapped to $+1$ or -1 depending on the majority of its neighbors. Fig. 8(b) is a linear-log plot of the data in Fig. 8(a), and again exhibits the characteristic exponential decay of the scaling function for the domain-size probability distribution. In this case, the numerical data for the three morphologies appears to be numerically comparable to that for the spin-1/2 Ising case.

Finally, Fig. 9 is a plot of characteristic domain scales for the *C* [Fig. 9(a)] and *D* [Fig. 9(b)] morphologies and is analogous to Fig. 6. For the *C* morphology, we show (i) length scales L_C and L_P for the *A*, *B* domains—obtained from the correlation function and the probability distribution, respectively; and (ii) the length scale L_D for the *V* domains obtained from the appropriate correlation function. Notice that the maximum length scale for the *V* domains in Fig. 9(a) is approximately 2 units, so the impression of growth is somewhat illusory. For the *D* morphology, we show the length scales L_C and L_P. In both cases, the length scales (apart from L_D) are consistent with a LS growth law.

V. SUMMARY AND DISCUSSION

Let us conclude this paper with a brief summary and discussion of the results presented here. We have undertaken a detailed MC study of phase-separation kinetics in ternary (ABC) mixtures. Without loss of generality, we focus on the ABV model, where one of the components (vacancy or V) is passive, i.e., pairwise interactions involving V's are identically zero. Furthermore, we consider constrained Kawasaki spin-exchange dynamics, where only $A\leftrightarrow V$, $B\leftrightarrow V$ interchanges are allowed but $A\leftrightarrow B$ interchanges are forbidden. However, we should clarify that we have also performed MC simulations with unconstrained dynamics, where all types of interchanges are permitted. The numerical results therefrom are very similar to those presented here upto a slight renormalization of time scales. This is because the barrier to $A\leftrightarrow B$ interchanges at domain interfaces (i.e., $E_B=12J$ in $d=2$) are considerably higher than those for $A\leftrightarrow V$ and $B\leftrightarrow V$ interchanges (i.e., $E_B=6J$ in $d=2$). Thus, especially at low temperatures, the segregation dynamics is primarily driven by V's—regardless of whether or not $A\leftrightarrow B$ interchanges are allowed.

In this paper, we focus on mixtures with composition $c_A=c_B=0.45$ and $c_V=0.1$. Nevertheless, our results are typical for a wide range of compositions. Our results demonstrate that there are three distinct evolution morphologies arising from a disordered initial condition—two-phase (AV-rich and BV-rich) coexistence; three-phase coexistence with coating (only AV and BV interfaces); and three-phase coexistence with blobs (all possible interfaces). We provide heuristic ar-

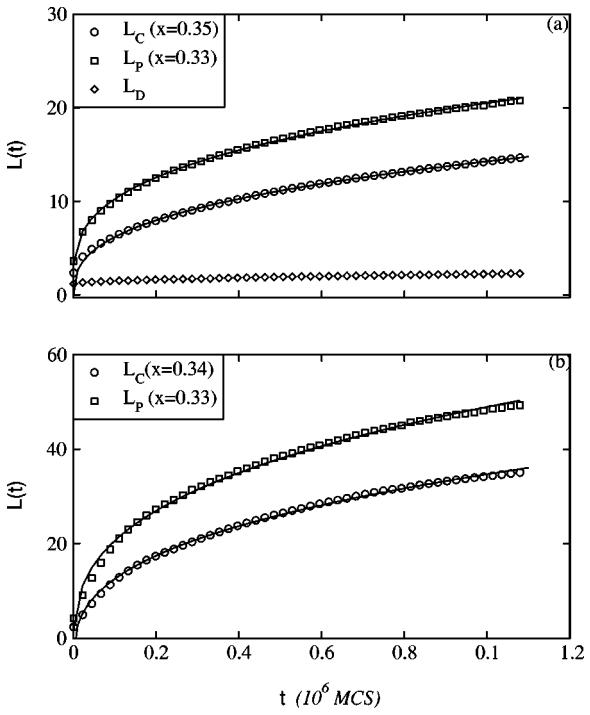

FIG. 9. (a) Characteristic length scales for the evolution depicted in Fig. 2(b). We plot $L(t)$ vs t for L_C, L_P, and L_D—denoted by the specified symbols. The nonlinear fits are obtained as in Fig. 6, and the corresponding best-fit exponents (x) are specified on the figure. (b) Analogous to (a), but for the evolution depicted in Fig. 2(c).

guments to understand the emergence of these morphologies at zero temperature, where entropic effects are not relevant. These arguments also clarify the nature of patterns observed in earlier simulations of ternary mixtures, in the context of *ABV* models and three-state Potts models. For nonzero temperatures, we expect the coating morphology to be asymptotically equivalent to the blob morphology for reasons we have discussed in Sec. IV.

We provide comprehensive numerical results for time-dependent behavior in all the three cases discussed above. There is a strong degree of universality in various dynamical properties, which we would like to highlight here. First, we expect the correlation functions to be asymptotically equivalent for the blob (B) and coat (C) morphologies; and for the dispersed (D) and Ising morphologies. Our numerical results for the correlation functions appear to point in this direction. Second, our numerical results suggest that the A-, B-domain-size distributions have similar scaling forms for all the morphologies considered. An important feature of the domain-size distribution is the exponential decay of the tail region—an observation we have also made earlier in the context of nonconserved domain growth [30]. We expect this to be a universal feature of phase-ordering systems with important implications for various properties, including the autocorrelation function. Third, the asymptotic domain growth law is always consistent with the LS law, $L(t) \sim t^{1/3}$, though the time scales of growth are substantially different in the three cases considered in this paper. This is because of the geometric constraints imposed by the availability of V's to facilitate diffusion.

Before concluding this paper, we should mention that we have also obtained numerical results for the autocorrelation function in our MC simulations. In earlier work on spin-1 models with local kinetic barriers [30], we have modeled spin dynamics using dichotomic Markov processes. We used this simple model to obtain an analytic expression for the autocorrelation function, which was in good agreement with our numerical results. At present, we are generalizing this approach to the context of vacancy-mediated phase separation in the *ABV* model. Details of this approach and comparisons with numerical results will be reported at a later stage [32].

ACKNOWLEDGMENTS

S.P. is grateful to K. Binder, P. Fratzl, J.-F. Gouyet, M. Plapp, and R. Weinkamer for many useful discussions regarding the problems addressed in this paper.

[1] J.D. Gunton, M. San Miguel, and P.S. Sahni, in *Phase Transitions and Critical Phenomena*, edited by C. Domb and J.L. Lebowitz (Academic Press, London, 1983), Vol. 8.
[2] K. Binder, in *Materials Science and Technology*, edited by R.W. Cahn, P. Haasen and E.J. Kramer (VCH, Weinheim, 1991), Vol. 5, p. 405,
[3] A.J. Bray, Adv. Phys. **43**, 357 (1994).
[4] I.M. Lifshitz and V.V. Slyozov, J. Phys. Chem. Solids **19**, 35 (1961).
[5] E.D. Siggia, Phys. Rev. A **20**, 595 (1979).
[6] J.F. Marko and G.T. Barkema, Phys. Rev. E **52**, 2522 (1995).
[7] C. Yeung, M. Rao, and R.C. Desai, Phys. Rev. E **53**, 3073 (1996).
[8] M. Blume, V.J. Emery, and R.B. Griffiths, Phys. Rev. A **4**, 1071 (1971).
[9] D. Mukamel and M. Blume, Phys. Rev. A **10**, 610 (1974).
[10] D. Furman, S. Dattagupta, and R.B. Griffiths, Phys. Rev. B **15**, 441 (1977).
[11] W. Hoston and A.N. Berker, Phys. Rev. Lett. **67**, 1027 (1991).
[12] J. Lajzerowicz and J. Sivardiere, Phys. Rev. A **11**, 2079 (1975); J. Sivardiere and J. Lajzerowicz, *ibid.* **11**, 2090 (1975).
[13] J.-F. Gouyet and M. Plapp, Ecole Polytechnique report, 1999 (unpublished).
[14] J.R. Manning, *Diffusion Kinetics for Atoms in Crystals* (Van Nostrand, Princeton, 1968).
[15] C.P. Flynn, *Point Defects and Diffusion* (Clarendon, Oxford, 1972).
[16] K. Yaldram and K. Binder, Z. Phys. B: Condens. Matter **82**, 405 (1991); J. Stat. Phys. **62**, 161 (1991); Acta Metall. Mater. **39**, 707 (1991).
[17] P. Fratzl and O. Penrose, Phys. Rev. B **50**, 3477 (1994); **53**, 2890 (1996).

[18] S. Puri, Phys. Rev. E **55**, 1752 (1997); S. Puri and R. Sharma, *ibid.* **57**, 1873 (1998).
[19] R. Sharma, Ph.D. thesis, Jawaharlal Nehru University, 1998.
[20] P.C. Hohenberg and B.I. Halperin, Rev. Mod. Phys. **49**, 435 (1977).
[21] L.P. Kadanoff and J. Swift, Phys. Rev. **165**, 310 (1968).
[22] B.I. Halperin, P.C. Hohenberg, and S.-K. Ma, Phys. Rev. B **10**, 139 (1974).
[23] M. Plapp and J.-F. Gouyet, Phys. Rev. Lett. **78**, 4970 (1997).
[24] C. Jeppesen and O.G. Mouritsen, Phys. Rev. B **47**, 14 724 (1993).
[25] G.S. Grest and P.S. Sahni, Phys. Rev. B **30**, 226 (1984).
[26] Y. Okabe, New J. Phys. **1**, 10.1 (1999).
[27] T. Kawakatsu, K. Kawasaki, M. Furusaka, H. Okaboyashi, and T. Kanaya, J. Phys.: Condens. Matter **6**, 6385 (1994).
[28] D. Chowdhury, J. Phys.: Condens. Matter **6**, 2435 (1994).
[29] R. Ahluwalia and S. Puri, J. Phys.: Condens. Matter **8**, 227 (1996).
[30] K. Tafa, S. Puri, and D. Kumar, Phys. Rev. E **63**, 046115 (2001).
[31] K. Binder and D. Stauffer, Phys. Rev. Lett. **33**, 1006 (1974).
[32] K. Tafa, D. Kumar, and S. Puri (unpublished).